Journal of Materials Chemistry A

PAPER

Cite this: J. Mater. Chem. A, 2015, 3, 1979

Nickel-mediated polyol synthesis of hierarchical V_2O_5 hollow microspheres with enhanced lithium storage properties†

Yan-Zhen Zheng,[abc] Haiyang Ding,[d] Evan Uchaker,[c] Xia Tao,*[ab] Jian-Feng Chen,[ab] Qifeng Zhang[c] and Guozhong Cao*[c]

Received 15th October 2014
Accepted 18th November 2014

DOI: 10.1039/c4ta05500d

www.rsc.org/MaterialsA

In this study, a facile template-free synthesis of hierarchical V_2O_5 hollow microspheres has been developed, based on a nickel-mediated polyol process and subsequent calcinations. It is found that morphological control over V_2O_5 micro-architecture is realized by adding Ni into the polyol process. XPS results demonstrate that Ni doping promotes the formation of low valence state vanadium in V_2O_5 samples and is beneficial to maintain electric stability to the V^{4+} state. Due to unique structure and low valence state vanadium in Ni–V_2O_5 microspheres, Ni (10 mol%)–V_2O_5 used as the cathode material for a lithium ion battery exhibits excellent lithium storage properties with very high capacity (294 mA h g^{-1}) and superior cycling stability and rate performance. The good electrochemical performance suggests that this hierarchical Ni–V_2O_5 material could be a promising candidate as a cathode material for lithium-ion batteries.

Introduction

Lithium ion batteries (LIBs) are attracting considerable interest as the predominant power source for portable electric devices, as well as the promising power source for electric vehicles (EVs) and hybrid electric vehicles (HEVs), owing to their high energy density, long lifespan, and environmental friendliness.[1–3] However, LIBs commercial use in EVs and HEVs is still hampered by their insufficient power density and poor rate performance. Thus, we are motivated to develop new competitively multifunctional electrode materials to meet increasing demands for the rapid development of portable electric devices, EVs as well as HEVs.[1–5] Vanadium oxides, especially orthorhombic vanadium pentoxide (V_2O_5), have been extensively investigated as high capacity cathode materials for next-generation LIBs in recent years, due to their high capacity (the theoretical capacity reaches 294 mA h g^{-1} when two lithium ions are intercalated), low cost, and abundant sources, together with ease of synthesis.[5–12] However, the practical application of V_2O_5 is still hindered by its low diffusion coefficient of Li^+ ions (10^{-13} to 10^{-12} cm^2 S^{-1}) and moderate electrical conductivity (10^{-3} to 10^{-2} cm^{-1}), together with poor structural stability.[13–15] To improve the diffusion capacity of Li^+ ions in V_2O_5, decreasing the particle size to nanoscale is commonly believed to be one of the most facile methods. Nanoscaled materials possessing high surface area and short diffusion paths could offer more electrochemically active sites, mitigate the concentration polarization of electrode materials, and accommodate the strain of Li intercalation/deintercalation.[5,7,11,16–22] To this end, various nanostructured V_2O_5, such as one-dimensional structures (nanowires, nanorods, and nanotubes),[21–23] nanosheets,[5] and nanofibers[12,24] have been fabricated to overcome their electrochemical kinetics disadvantage. For example, leaf-like V_2O_5 nanosheets were prepared to be cathode materials for LIBs, showing very high rate capacity of 303 mA h g^{-1} and 104 mA h g^{-1} at current densities of 50 and 5000 mA g^{-1}, respectively.[5] Nevertheless, most of nanostructured V_2O_5 electrodes suffer from safety hazards and severe capacity fading upon prolonged cycling owing to the increasing contact between the electrolyte and large-surface-area nanomaterials. Indeed, micro-sized spherical particles with compact configuration, as commercial electrode materials in LIBs, exhibit high volumetric energy density and excellent rate capacity. As such, 3D hierarchical nano/micro-configurations such as hollow microspheres and hierarchical microflowers have been anticipated to be superior electrode materials for synchronously inheriting the merits of

[a]State Key Laboratory of Organic-Inorganic Composites, Beijing University of Chemical Technology, Beijing 100029, China. E-mail: taoxia@yahoo.com; Fax: +86-10-64434784; Tel: +86-10-64453680

[b]Research Center of the Ministry of Education for High Gravity Engineering & Technology, Beijing University of Chemical Technology, Beijing 100029, China. Fax: +86-10-64434784; Tel: +86-10-64446466

[c]Department of Materials Science and Engineering, University of Washington, Seattle, WA 98195, USA. E-mail: gzcao@u.washington.edu

[d]General Research Institute for Nonferrous Metals, Beijing 100088, China

† Electronic supplementary information (ESI) available: EDS of Ni–V_2O_5 microspheres. (Fig. S1) SEM images of V_2O_5 samples. (Fig. S2) N_2 adsorption–desorption isotherm and corresponding BJH pore-size distribution curves of Ni–V_2O_5. (Fig. S3) The first three consecutive CVs of the Ni–V_2O_5 hollow microspheres at a scan rate of 0.2 mV s^{-1}. See DOI: 10.1039/c4ta05500d

the nano- and micro-structured materials, in which the primary nano-sized building blocks could guarantee Li^+ ion transport, and the robust secondary micro-sized architectures could effectively avoid self-aggregation and structure degradation upon cycling.[8–10,24–30] More attractively, the inter-particle pore network in the complex hierarchical architectures could facilitate electrolyte penetration and simultaneously permit accommodation of large volume variation during charging–discharging processes.

A common synthetic strategy for the fabrication of hollow microspherical V_2O_5 employs a mediated polyol process with the help of organic surfactants *i.e.* poly(vinylpyrrolidone) (PVP), in which PVP has great influence on the morphologies of vanadium precursors.[24] The addition of some inorganic species such as Fe^{2+}, Fe^{3+}, and $NaNO_3$ has been demonstrated to be able to play a dramatic role analogy to organic surfactants on controlling the shape of metallic and metal oxide nanoparticles.[31] Furthermore, introducing alien species into V_2O_5 represents another efficient approach to further improve the electrochemical properties of active materials. A variety of studies have demonstrated that incorporating carbon or conductive polymer,[11,32] as well as doping with transition metal ions,[11,33–39] could effectively increase electrical conductivity and hence enhance Li ion intercalation properties. As successful examples, doping Ag and Cu in V_2O_5 have been verified to be able to enhance electronic conductivity by two or three orders of magnitude.[33,37] Lower valence vanadium ions (V^{4+}) and oxygen vacancies, which are reported to be beneficial to enhance the conductivity and cyclic stability of LIBs, could be effectively produced by means of doping Mn or Sn into a V_2O_5 matrix.[37,39] Ni inserting into a V_2O_5 lattice could improve the electrochemical insertion process of lithium ions and hence enhance capacity and electrochemical reversibility. Moreover, it was found that Ni doping in MnO_2 matrix could improve electrochemical performance of cathode materials by offering electric stability to the Mn^{3+} state and mitigate Jahn–Teller distortion.[40] Encouraged by the benefit of 3D hierarchical structure and alien cation doping, we are motivated to develop a facile template-free nickel-mediated polyol process to prepare a high performance V_2O_5 hollow microsphere for LIBs, in which nickel acts not only as mediator to tailor the interior hollow structures of V_2O_5 and build favorable 3D hierarchical nano-micron combined architecture, but also as doping units to tune vanadium valence states and improve lithium storage properties.

Experimental section

Hollow V_2O_5 microspheres were prepared by a simple nickel-mediated polyol route followed by thermal treatment. Briefly, 0.01 mol ammonium metavanadate (NH_4VO_3) and 0.001 mol nickel acetate ($NiAc_2 \cdot 4H_2O$) were added to 50 mL ethylene glycol ($H_2C_6O_2$, VWR). The mixed solution was heated to 180 °C in an oil bath at a rate of 5 °C min^{-1} and then refluxed for 3 h, after which it was cooled naturally. Following precipitate centrifuging, washing and drying, the final products (Ni–V_2O_5) were annealed at 600 °C for 2 h in air. For comparison, pure V_2O_5 sample (V_2O_5) was obtained by following the same procedure described for the Ni–V_2O_5 material, the only difference in the synthesis being represented by the starting reactant by mixing 0.01 mol NH_4VO_3 in 50 mL $H_2C_6O_2$.

The phase and crystallite size of the Ni–V_2O_5 microspheres were identified using X-ray diffraction (XRD, D8 Bruker X-ray diffractometer) with Cu Kα radiation within the range of 10°–70° (2θ). The accelerating voltage and current were 40 kV and 40 mA, respectively. The morphology of V_2O_5 and Ni–V_2O_5 samples were characterized using field-emission scanning electron microscopy (FESEM, JEOL JSM-7000F), and the nanostructure was investigated using transmission electron microscopy (TEM, FEI Tecnai G2 F20).

Nitrogen adsorption–desorption isotherms were measured using Quantachrome NOVA 4200e system. Samples were degassed at 100 °C overnight under vacuum prior to measurements. The specific surface area and micropore and mesopore volumes were determined by multipoint Brunauer–Emmett–Teller (BET), *t*-method, and Barrett–Joyner–Halenda (BJH) desorption analyses, respectively.

X-ray photoelectron spectroscopy (XPS) was used to determine the oxidation state of vanadium and nickel in the doping samples. XPS spectra were taken on a Surface Science Instruments S-probe spectrometer. This instrument has a monochromatized Al Kα X-ray and a low-energy electron flood gun for charge neutralization. The X-ray spot size for these acquisitions was approximately 800 μm and the take-off angle (the angle between the sample normal and the input axis of the energy analyzer) was about 55° (55° degree take-off angle 50–70 Å sampling depth). Pressure in the analytical chamber during spectral acquisition was less than 5×10^{-9} Torr. Pass energy for survey spectra was 150 eV, and the pass energy for the high-resolution scans was 50 eV. Data analyses were performed using the Service Physics ESCA Hawk 7 Data Analysis Software (Service Physics, Bend, OR). Three spots were tested on each sample to make final results credible.

Contact angles were measured with the static sessile drop method by a VCA Optima goniometer. All measurements were performed with V_2O_5 and Ni–V_2O_5 powder samples mixed with super 20.0 wt% P conductive carbon (TIMCAL Graphite & Carbon), and 10.0 wt% polyvinylidene fluoride (PVDF) binder in a *N*-methyl-2-pyrrolidone (NMP, Alfa Aesar) solvent that had been spread onto aluminum foil to form film. Surfaces were wet using ~1 μL of DI water and analyzed immediately after the droplet touched the sample. Multiple droplets were placed on each sample surface at different spots in order to avoid remeasuring an area that had already been wet. VCR Optima XE software was used to measure angles on both the left and right sides of the droplet, and the average angle was calculated.

The electrochemical properties of the Ni–V_2O_5 microspheres were tested in coin-type cells, which were assembled in an argon-filled glove-box. The cathode slurry was prepared by dispersing the Ni–V_2O_5 or V_2O_5 sample, super P conductive carbon, and PVDF binder in a NMP solvent at a respective weight ratio of 70 : 20 : 10. The slurry was then spread onto aluminum foil current collector and dried in a vacuum oven at 80 °C overnight. The mass loading was around 0.2 mg. Lithium metal foil, 1 M $LiPF_6$ in ethylene carbonate (EC)/dimethyl

carbonate (DMC) (1 : 1 v/v), and Celgard 2400 membrane were used as the counter electrode, electrolyte, and separator, respectively. Galvanostatic charging–discharging and cycle stability performance of V_2O_5 and doped V_2O_5 microspheres were characterized using Land-CT2001A battery tester at room temperature. Cyclic voltammetry (CV) was measured using an electrochemical analyzer (Solartron 1287A) in the voltage range of 2.0–4.0 V (*vs.* Li/Li^+) with a scanning rate of 0.2 mV s^{-1}. Electrochemical impedance spectroscopies (EIS) were performed on the Solartron 1287A in conjunction with a Solartron 1260FRA/impedance analyzer. The frequency range was explored from 100 mHz to 100 kHz and the AC amplitude was 10 mV.

Results and discussion

The representative XRD patterns, as shown in Fig. 1a with the peaks labeled, examine the crystal phase and crystallinity of the V_2O_5 and Ni–V_2O_5 samples. All the clear diffraction peaks of both Ni–V_2O_5 and V_2O_5 samples are in good agreement with the standard pattern of the orthorhombic V_2O_5 phase (JCPDS card no. 41-1426).[30,39] No other secondary phases could be detected in the patterns of the Ni–V_2O_5 sample. Additionally, the diffraction peak height of the Ni–V_2O_5 sample is much lower than that of the pure V_2O_5 sample, indicating that Ni doping decreases the crystal size of V_2O_5. The crystallite size is estimated around 23.3 nm for Ni–V_2O_5 nanoparticles, much smaller than that of the V_2O_5. The lattice constants are a = 11.478, b = 3.583, and c = 4.362 for pure V_2O_5,[41,42] and a = 11.512, b = 3.567, and c = 4.386 for Ni–V_2O_5. In comparison with V_2O_5, small lattice expansion along both *a*- and *c*-axes and slight compression along the *b*-axis are found for Ni–V_2O_5, suggesting Ni successfully doping into V_2O_5 crystal structure. From the difference of lattice constants between V_2O_5 and Ni–V_2O_5, it can be inferred that the Ni^{2+} ions are likely to lie between the VO_5 slabs and be 4-fold coordinated by apical oxygen of four [NiO_6] octahedra.[43,44] The introduction of Ni^{2+} is thought to be able to stabilize the VO_5 layers, and hence probably be beneficial to improve intercalation/extraction property of Li^+ within the layers of V_2O_5.

The oxidation state of vanadium in the V_2O_5 and Ni–V_2O_5 electrodes are investigated *via* XPS measurement, and the results are provided in Fig. 2a and b. The V 2p3/2 core peak spectra of both V_2O_5 and Ni–V_2O_5 samples display two components centered at 518.0 and 516.5 eV, which is ascribed to two formal oxidation degrees of V^{5+} and V^{4+}, respectively.[45] From the relative areas of the V^{5+} and V^{4+} contributions, the molar ratio of $V^{4+}/(V^{4+} + V^{5+})$ is 6% for the Ni–V_2O_5, which is 50% higher than that (4%) of V_2O_5. Therefore, Ni doping promotes the formation of low valence state vanadium in V_2O_5 samples and is beneficial to maintain electric stability to V^{4+} state, which has been verified in Ni doped MnO_2 matrix.[40] As reported in literature,[46] on one hand, low valence state V^{4+} could improve the conductivity of the V_2O_5 film, and hence facilitate the Li^+ intercalation/deintercalation within V_2O_5 film; on the other hand, the radius of V^{4+} (0.86 Å) is much larger than that of V^{5+} (0.495 Å), which is favorable for accommodation of volumetric variation accompanying with the reduction of V^{5+} to V^{4+} during intercalation. Moreover, oxygen vacancies may arise to maintain the charge neutrality when V^{5+} reduces to V^{4+}, which could serve as nucleation centers for phase transformation during lithium ion intercalation/deintercalation processes.[37] The presence of oxygen vacancies is beneficial to the formation of more open structure and easy access for lithium ion intercalation and diffusion.[37,47] For the Ni–V_2O_5 sample, the two components at ~856 eV (Ni 2d1/2) and 861.7 eV (Ni 2d3/2) are associated with the Ni(II) oxide (see Fig. 2c), indicating that the Ni atoms in Ni–V_2O_5 is in a 2+ formal oxidation state.[48] Furthermore, according to literature:

$$E_0(V^{5+}/V^{4+}) = 0.991\ \text{V},\ E_0(Ni^{3+}/Ni^{2+}) = 2.56\ \text{V} \quad (1)$$

The potential of $E_0(V^{5+}/V^{4+})$ is much lower than that of $E_0(Ni^{3+}/Ni^{2+})$, therefore it is unlikely for V^{4+} and Ni^{3+} to coexist in the structure of vanadium oxide. It further verifies that the valence state of nickel exists in divalence (Ni^{2+}) in Ni–V_2O_5.

Fig. 3a and b show the FESEM images of Ni–V_2O_5 after calcination. The low magnification FESEM image shows that it consists of hierarchically structured Ni–V_2O_5 monodispersed microspheres with a diameter of around 4 μm (Fig. 3a). From

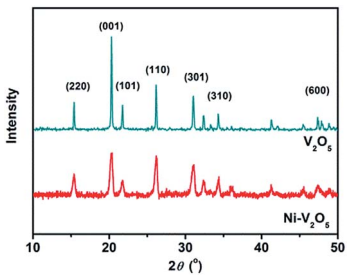

Fig. 1 XRD patterns of the pure V_2O_5 and Ni–V_2O_5.

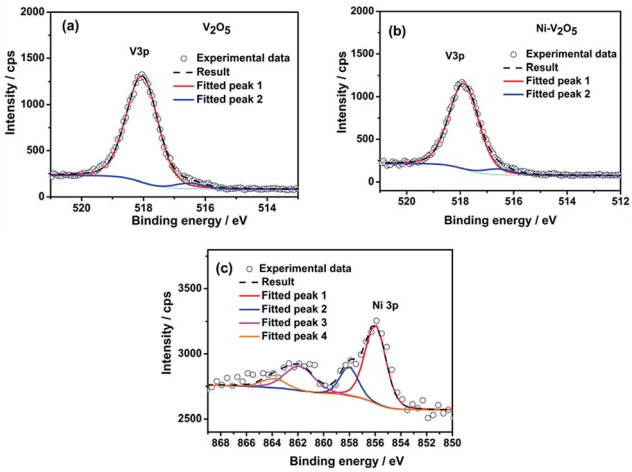

Fig. 2 XPS spectra of high-resolution scan on the V $2p_{3/2}$ core peaks performed on the (a) pure V_2O_5 and (b) Ni–V_2O_5, together with (c) the Ni$2p_{3/2}$ core peak of Ni–V_2O_5.

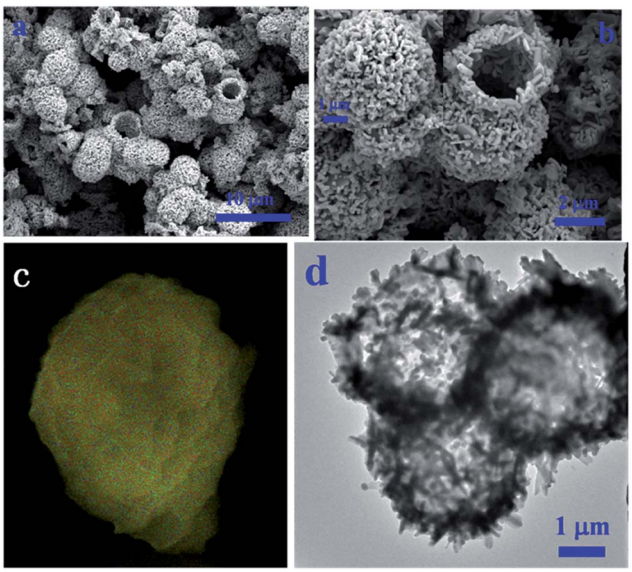

Fig. 3 SEM (a & b), elemental mapping (c) and TEM (d) images of Ni–V_2O_5 microspheres. Note: green, red and blue represent O; V and Ni respectively.

the broken microspheres, one can clearly observe that microspheres have hollow interiors. The interlinking growth between two hollow microspheres tends to form a gourd-like shape with ~500 nm thickness shell. The magnified FESEM image, as shown in Fig. 3b, further reveals that the detailed surface morphology of microspheres are stacked with small nanoplates with a thickness of ~200 nm and a small portion of nanoparticles of about 100 nm. This will endow the electrode material with shorter diffusion pathways and easier Li^+-electron transport, resulting in enhanced electrochemical properties. Energy dispersive spectroscopy (EDS), as shown in Fig. S1,† reveals that the Ni/V molar ratio is 8.5%, which is similar to the value (8.1%) provided by XPS. The overall composition and spatial distribution of Ni in an individual sphere was further investigated by SEM elemental mapping. Fig. 3c and S2† show bright-field SEM images of Ni–V_2O_5 spheres and the elemental mapping for Ni, O and V atoms. The homogeneous spatial distribution of Ni dopant within the sample is clearly discernible. A FESEM image of V_2O_5 is presented in Fig. S3a (ESI†). It can be found that plate-like V_2O_5 are loosely aggregated over a large domain to form porous irregular architecture. In a high-magnification FESEM image (Fig. S3b (ESI†)), it can be easily found that the V_2O_5 plates have a length from 200 nm to 1 μm and a thickness of ~80 nm.

In the polyol process, EG serves as both the solvent and reducing reagent, which has been widely introduced to prepare metal nanoparticles with controllable structures.[31,49,50] Xia and co-workers proposed that the formation of nanoparticles in the presence of EG involves two key steps: (i) coordination of EG to the central metal ion to form a metal glycolate, and (ii) subsequent oligomerization.[50] The reaction between NH_4VO_3 and EG has been reported to produce vanadyl glycolate.[30,51] Then, nickel-doped vanadyl glycolate nanoparticles with a bimodal size distribution would form *via* a self-seeding process, followed by subsequent homogeneous and heterogeneous nucleation. In the process of refluxing, the nanoparticles having larger size grow at the expense of small counterparts (Ostwald ripening).[50] In this work, as for the formation of the hollow microsphere structure, we briefly propose that two key steps are involved: (i) the formation of Ni-doped vanadyl glycolate nanoparticles *via* a self-seeding process; (ii) the formation of hollow microsphere morphology *via* the aggregation reaction, in which the Ni-doped vanadyl glycolate nanoparticles aggregate around the N_2 microbubbles produced during the reaction in an attempt to minimize their interfacial energy.[30] However, it is worth pointing out that the void within hollow-structured Ni–V_2O_5 microspheres in this work is larger than that within hollow V_2O_5 ones previously prepared *via* a solvothermal route in sealed PTFE lined stainless steel autoclave for 24 h at 180 °C,[30] owing to different pressures in the two reaction containers. The pressure within the unsealed container (this work) is lower than that within the sealed one (PTFE lined stainless steel autoclave), and the volume of N_2 microbubbles is larger within the former one, resulting in larger hollow interiors. Moreover, a portion of Ni^{2+} could be readily reduced to Ni^0 by the EG reducing agent. The function of the intermediate Ni^0 is to reduce V^{5+} to V^{4+} and serve as a catalyst to accelerate the formation of vanadyl glycolate. Thus, the presence of $Ni(AC)_2$ in the starting agents not only dopes in the vanadyl glycolate chain, but also significantly accelerates the reduction reaction (3 h) and growth of plate-like nanocrystals, which is beneficial to form a thin and compact shell of Ni doped V_2O_5 hollow microspheres.

The formation of the Ni–V_2O_5 hollow microsphere is further evidenced by transmission electron microscopy (TEM) images, as shown in Fig. 3d. The microspheres show a hollow interior of ~3 μm as demonstrated by the distinct brightness contrast in the central region. The hierarchical hollow structure loosely assembled from nanoplates with thickness of ~200 nm and nanoparticles with the diameter ranged from 50 to 100 nm. The shell thickness of the microsphere is ~500 nm, which is thick enough to support the rigid hierarchical hollow structure. Nitrogen adsorption–desorption isotherm measurement was performed, and the results were displayed in Fig. S4 (ESI†). The hollow microspheres give rise to a moderate BET surface area of 25.2 $m^2 g^{-1}$, larger than that of the pure V_2O_5 sample (13.8 $m^2 g^{-1}$). The BJH pore size distribution obtained from isotherm shows that the Ni–V_2O_5 sample contains mesoscale pores, the majority of which are in the 6–9 nm size range. Such mesoscale pores are related to the interparticle or interplate voids within the shell. The relatively large surface area and mesoscale sized pores of the as-synthesized porous Ni–V_2O_5 nanoarchitectures guarantee short Li-ion diffusion distances and hence hold the capacity of improving the electrochemical kinetics.

The wettability of the active material surface is a vital factor to reflect the interaction between the electrolyte and the active electrode material. Contact angles were characterized to assess how Ni doping affects the surface properties of the V_2O_5 sample. All the samples used for contact angle measurements were rolled into sheets for making electrodes. As shown in Fig. 4a and b, compared with V_2O_5 (135°), Ni–V_2O_5 (115°) has a smaller

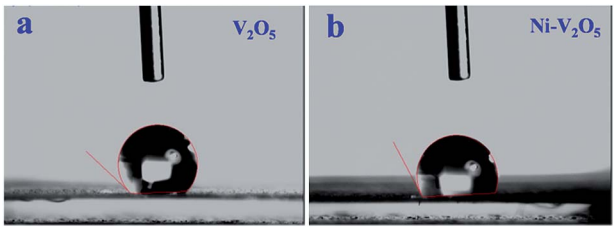

Fig. 4 Images showing the wettability of (a) pure V_2O_5 and (b) Ni–V_2O_5 electrodes.

contact angle, indicating a better wettability for Ni–V_2O_5. This means that Ni doping greatly improves wetting behavior of V_2O_5 samples, hence leading to facile and sufficient contact between electrolyte and Ni–V_2O_5 electrode. The enhanced wettability of Ni–V_2O_5 could be explained by assuming that Ni doping promotes the formation of low valence state V^{4+} and hence oxygen vacancies are created at the surface to maintain the charge neutrality. The produced oxygen vacancies are presumably favorable for electrolyte infiltration. Generally, electrolyte is dissociatively adsorbed on defect sites to form a highly hydrophilic surface. Thus, the wettability of Ni–V_2O_5 is enhanced.[52]

The electrochemical properties of Ni–V_2O_5 hollow microspheres are evaluated by cyclic voltammetry. Fig. 5a shows the cyclic voltammograms (CVs) of the LIB fabricated from V_2O_5 and Ni–V_2O_5 hollow microspheres in the voltage region of 2.0–4.0 V *vs.* Li/Li^+ at a scan rate of 0.2 mV s^{-1}. Three dominant cathodic peaks, appearing at 3.32, 3.12, and 2.22 V, are observed for the V_2O_5 electrode, indicating the multi-step lithium ion insertion process. The insertion of the first Li^+ ion into V_2O_5 undergoes a two-step lithium ion insertion process and correspondingly the two cathodic peaks at 3.32 and 3.12 V attribute to phase transitions from α-V_2O_5 to ε-$Li_{0.5}V_2O_5$ and then to δ-LiV_2O_5, respectively. The second Li^+ ion is inserted through one single step around 2.22 V, resulting in the formation of

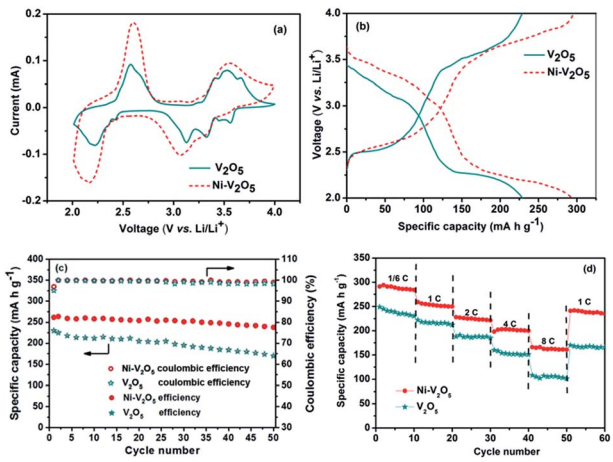

Fig. 5 (a) CV curves obtained at a scan rate of 0.2 mV s^{-1}; (b) charging–discharging curves; (c) cycle stability and coulombic efficiency over 50 cycles at 300 mA g^{-1}; and (d) discharging-rate capability at various densities for pure V_2O_5 and Ni–V_2O_5 electrodes.

γ-$Li_2V_2O_5$.[8] Accordingly, three observed anodic peaks at the potentials of 2.57, 3.40 and 3.51 V are ascribed to the Li^+ ion deintercalation process, corresponding to the reverse phase transformations from γ-$Li_2V_2O_5$ to δ-LiV_2O_5, ε-$Li_{0.5}V_2O_5$, and α-V_2O_5, respectively. Apart from the major redox peaks, a pair of minor redox peaks located at 3.63 V and 3.56 V could also be found in the V_2O_5 electrode, which is associated with structural changes.[38] As for the Ni–V_2O_5 electrode, two pairs of well-defined redox peaks located around 3.54 V/3.07 V and 2.59 V/2.17 V could be observed in the CV curve. Moreover, it is worth noting that the Ni–V_2O_5 electrode shows a broad oxidation/redox peak around 3.54 V/3.07 V, probably owing to a slightly poor crystallinity and small lattice expansion along both *a*- and *c*-axes of V_2O_5. The symmetrical feature of the CV curves implies a good reversibility of the cycling process (see Fig. S5†). This means that the number of phase transitions decreases and the irreversible phase transitions as well as structural changes occurred in Ni–V_2O_5 electrode are effectively suppressed.[37] The presence of surface defects originating from Ni doping increases surface energy and could possibly serve as a nucleation center, thus facilitating phase transitions and achieving better reversibility and stability of the cycling process. A similar phenomenon was also observed for Mn-doped V_2O_5 and Cu-doped V_2O_5.[37,47]

Fig. 5b exhibits the representative discharge and charge curves of the V_2O_5 and Ni–V_2O_5 electrode measured at a constant current density of 50 mA g^{-1} within a voltage window of 2.0–4.0 V. For the V_2O_5 electrode, two plateaus at approximately 3.31 and 3.11 V are associated with the phase transitions from α-V_2O_5 to ε-$Li_{0.5}V_2O_5$ and from ε-$Li_{0.5}V_2O_5$ to δ-LiV_2O_5, respectively. The third clear plateau observed at ~2.27 V is related to the formation of the γ-$Li_2V_2O_5$, which originates from the intercalation of the second lithium ion into δ-LiV_2O_5.[8] As for the Ni–V_2O_5 electrode, two poorly defined voltage plateaus observed in the discharge–charge curves are well consistent with the two dominant redox peaks in the CV curves, corresponding to more facile electrochemical reactions among the transitional phases. The initial capacity of V_2O_5 and Ni–V_2O_5 electrodes are 229 and 294 mA h g^{-1}, respectively. Additionally, Ni–V_2O_5 electrodes with different Ni doping amounts (5 mol% and 15 mol%) are also examined, and the obtained initial capacities are 265 and 282 mA h g^{-1}, respectively. The effects of Ni doping amounts on the electrochemical performance of V_2O_5-based LIBs will be investigated in detail in the following research.

The cycling behavior of the V_2O_5 and Ni–V_2O_5 hollow microspheres at a current density of 300 mA g^{-1} that amounts to a rate of 1 C is displayed in Fig. 5c. For Ni–V_2O_5, the initial capacity is 262 mA h g^{-1}, and then the value slightly increases to 264 mA h g^{-1} in the second cycle probably originating from sufficient electrolyte penetration. The specific discharge capacity could still be retained 238 mA h g^{-1} at the end of 50th cycle, with a capacity retention of 91% of the initial capacity. The capacity fading rate is about 0.20% per cycle, which is lower than the result reports for V_2O_5 electrodes.[8,38] The cycling performance of V_2O_5 is also presented for comparison, which shows inferior capacity retention (85%). This suggests that Ni

doping leads to a significant improvement on cycling stability. On the one hand, the occupancy of Ni^{2+} is able to expand the V_2O_5 lattice and stabilize the VO_5 layers, and thus facilitate improving the intercalation/extraction property of Li^+ within the layers of V_2O_5. On the other hand, low valence state vanadium (V^{4+}) and oxygen vacancies in the Ni–V_2O_5 electrode have better capability to mitigate volumetric variation during the Li^+ ion insertion and removal processes. For the Ni–V_2O_5 electrode, the coulombic efficiency remains close to 100% during the cycling tests, indicating excellent reversibility of the electrodes.

The rate performance of the Ni–V_2O_5 is shown in Fig. 5d and confirms a more facile Li ion intercalation/deintercalation within the hollow microsphere nanostructured Ni–V_2O_5 as compared with V_2O_5. In general, Ni–V_2O_5 shows a higher capacity than V_2O_5 at each current rate mentioned in this work. The Ni–V_2O_5 delivers a discharge capacity of 294 mA g h^{-1} at a current density of 50 mA g^{-1} (1/6 C) in the 2nd cycle, which maintains at ~284 mA h g^{-1} after 10 cycles. It delivers specific discharge capacities of 259, 228, 203, and 166 mA h g^{-1} at 1 C, 2 C, 4 C and 8 C, respectively. When cycled at a high rate of 8 C, a capacity of only 108 mA g h^{-1} is delivered by the V_2O_5 electrode under the same conditions. Furthermore, the Ni–V_2O_5 could recover a high capacity, *i.e.* 242 mA h g^{-1}, which is almost the same as initial capacity when the current rate is decreased back to 1 C, indicating facile Li^+ ions intercalation/extraction in Ni–V_2O_5 hollow microspherical architecture. For V_2O_5, the capacity decreases in the first ten cycles under the discharge current of 1/6 C, and then drops slightly when the current increases from 1/6 C to 1 C. The probable reason is that the poor porous structure of the undoped V_2O_5 electrode results in a hard lithium ion intercalation process under a low discharge current of 1/6 C. The rate capacity for Ni–V_2O_5 is far better than that of V_2O_5 and also exhibits a moderate improvement when compared with some previous reports on V_2O_5 nanorods, nanoparticles, and hollow spheres.[30,32,52] The prominent electrochemical properties of such Ni–V_2O_5 hollow microspheres are probably originating from Ni doping as well as the robust shell of the hollow microsphere in several aspects. First, Ni^{2+} doping improves wetting behavior of V_2O_5, and hence facilitates the electrolyte to transport the intercalation/extraction within the layers of V_2O_5. Second, the nanoscaled building blocks within the shell are beneficial to the transportation of Li^+ ions and electrons; moreover, the sufficient void space within the microspheres and the porous shell provide sufficient contact area to guarantee efficient electrolyte penetration within the electrode. Finally, 3–5 μm-sized spheres could effectively inhibit the aggregation of the primary nanoparticles and their dissolution into the electrolytes.

To investigate the influence of Ni doping on the electrochemical kinetics of the Li^+ intercalation/deintercalation process within V_2O_5 electrodes, EIS measurement was performed over a frequency range of 100 kHz to 0.1 Hz (see Fig. 6). The Nyquist plot of the Ni-doped electrode displays a semicircle in the high frequency region and a straight line in the low frequency range. The semicircle at the high frequency region associates with the combined process of surface film (R_{sf}) and the charge transfer resistance (R_{ct}). The R_{sf+ct} values,

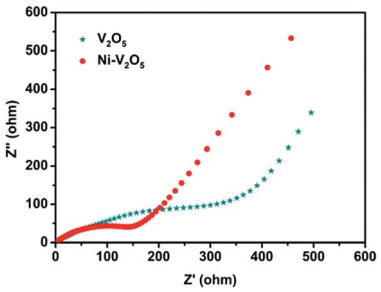

Fig. 6 EIS plots of V_2O_5 and Ni–V_2O_5 electrodes.

determined by the diameter of the semicircle at high frequency, are 378 Ω for V_2O_5, and 149 Ω for Ni–V_2O_5, respectively. The lower R_{sf+ct} value demonstrates improved conductivity of Ni–V_2O_5, which is likely to result from the presence of lower valence vanadium ions (V^{4+}) within Ni–V_2O_5. Furthermore, such a prominent decrease in R_{sf+ct} value suggests that the electrochemical reaction within the Ni–V_2O_5 electrode becomes much easier than that within the V_2O_5 electrode. In previous works, we have demonstrated that the presence of surface defects including V^{4+} and oxygen vacancies could reduce the charge-transfer resistance meanwhile preventing active electrode material from dissolution in the electrolyte, hence improving cyclic stability.[37,39]

Conclusions

In summary, uniform Ni–V_2O_5 hollow microspheres consisting of a hierarchical arrangement of nanoplates surrounding a central hollow bubble have been successfully synthesized by a Ni-mediated polyol method followed by heat treatment in air. Ni–V_2O_5, as a cathode material for LIBs, exhibits high initial reversible capacities of 294 mA h g^{-1} and 264 mA h g^{-1} at the current density of 50 and 300 mA h g^{-1}, respectively. Such Ni–V_2O_5 possessing of moderate BET surface area, porous structure, and better wetting ability, leads to excellent C-rate capability and good cycling stability compared to undoped V_2O_5. Therefore, Ni–V_2O_5 with improved electrochemical performance may be developed as a promising cathode material for high-capacity LIBs.

Acknowledgements

This research has been financially supported in part by the National Science Foundation (NSF, CMMI-1030048) and the University of Washington TGIF grants. Portions of this work were performed at the University of Washington NanoTech User Facility, a member of the NSF National Nanotechnology Infrastructure Network (NNIN). Yan-Zhen Zheng also sincerely appreciates the financial support in part of sponsorship from the National Science Foundation of China (NSFC) (21476019), Beijing Higher Education Young Elite Teacher Project (YETP0487), 863 project (2013AA031901), and the China Scholarship Council (CSC).

Notes and references

1 Q. F. Zhang, S. L. Candelaria, E. Uchaker and G. Z. Cao, *Chem. Soc. Rev.*, 2013, **42**, 3127–3171.
2 P. G. Bruce, S. A. Freunberger, L. J. Hardwick and J. M. Tarascon, *Nat. Mater.*, 2012, **11**, 19–29.
3 E. Uchaker, M. Gu, N. Zhou, Y. Li, C. Wang and G. Cao, *Small*, 2013, **9**, 3880–3886.
4 M. Zhang, Y. Li, E. Uchaker, S. Candelaria, L. Shen, T. Wang and G. Cao, *Nano Energy*, 2013, **2**, 769–778.
5 Y. li, J. Yao, E. Uchaker, J. Yang, Y. Huang, M. Zhang and G. Cao, *Adv. Energy Mater.*, 2013, **9**, 1171–1175.
6 Y. Wang and G. Z. Cao, *Adv. Mater.*, 2008, **20**, 2251–2269.
7 Y. L. Cheah, R. V. Hagen, V. Aravindan, R. Fiz, S. Mathur and S. Madhavi, *Nano Energy*, 2013, **2**, 57–64.
8 A. Pan, H. B. Wu, L. Yu and X. W. Lou, *Angew. Chem., Int. Ed.*, 2013, **52**, 2226–2230.
9 C. Zhang, Z. Chen, Z. Guo and X. W. Lou, *Energy Environ. Sci.*, 2013, **6**, 974–978.
10 A. Pan, H. B. Wu, L. Zhang and X. W. Lou, *Energy Environ. Sci.*, 2013, **6**, 1476–1479.
11 L. Mai, F. Dong, X. Xu, Y. Luo, Q. An, Y. Zhao, J. Pan and J. Yang, *Nano Lett.*, 2013, **13**, 740–745.
12 C. Gerbaldi, M. Destro, J. R. Nair, S. Ferrari, I. Quinzeni and E. Quartarone, *Nano Energy*, 2013, **2**, 1279–1286.
13 M. S. Whittingham, *Chem. Rev.*, 2004, **104**, 4271–4301.
14 F. Lantelme, A. Mantoux, H. Groult and D. Lincot, *J. Electrochem. Soc.*, 2003, **150**, A1202–A1208.
15 S. D. Perera, B. Patel, N. Nijem, K. Roodenko, O. Seitz, J. P. Ferraris, Y. J. Chabal and K. J. Balkus Jr, *Adv. Energy Mater.*, 2011, **1**, 936–945.
16 K. Takahashi, Y. Wang and G. Cao, *J. Phys. Chem. B*, 2005, **109**, 48–51.
17 P. G. Bruce, B. Scrosati and J. M. Tarascon, *Angew. Chem., Int. Ed.*, 2008, **47**, 2930–2946.
18 Y. S. Hu, X. Liu, J. O. Muller, R. Schlogl, J. Maier and D. S. Su, *Angew. Chem., Int. Ed.*, 2009, **48**, 210–214.
19 T. Y. Zhai, H. M. Liu, H. Q. Li, X. S. Fang, M. Y. Liao, L. Li, H. S. Zhou, Y. Koide, Y. Bando and D. Golberg, *Adv. Mater.*, 2010, **22**, 2547–2552.
20 Y. Wang, H. J. Zhang, W. X. Lim, J. Y. Lin and C. C. Wong, *J. Mater. Chem.*, 2011, **21**, 2362–2368.
21 H. M. Liu and W. S. Yang, *Energy Environ. Sci.*, 2011, **4**, 4000–4008.
22 Y. Wang, K. Takahashi, H. M. Shang and G. Z. Cao, *J. Phys. Chem. B*, 2005, **109**, 3085–3088.
23 Y. Wang and G. Z. Cao, *Chem. Mater.*, 2006, **18**, 2787–2804.
24 A. M. Cao, J. S. Hu, H. P. Liang and L. J. Wan, *Angew. Chem., Int. Ed.*, 2005, **44**, 4391–4395.
25 J. Liu, H. Xia, D. F. Xue and L. Lu, *J. Am. Chem. Soc.*, 2009, **131**, 12086–12087.
26 Q. Pan, T. Zhu, H. B. Wu and X. W. Lou, *Chem.–Eur. J.*, 2013, **19**, 494–500.
27 X. Rui, J. Zhu, D. Sim, C. Xu, Y. Zeng, H. H. Hng, T. M. Lim and Q. Yan, *Nanoscale*, 2011, **3**, 4752–4758.
28 D. Yu, C. Chen, S. Xie, Y. Liu, K. Park, X. Zhou, Q. Zhang, J. Li and G. Cao, *Energy Environ. Sci.*, 2011, **4**, 858–861.
29 J. Liu, Y. Zhou, J. Wang, Y. Pan and D. Xue, *Chem. Commun.*, 2011, **47**, 10380–10382.
30 E. Uchaker, N. Zhou, Y. Li and G. Cao, *J. Phys. Chem. C*, 2013, **117**, 1621–1626.
31 L. Mai, L. Xu, C. Han, X. Xu, Y. Luo, S. Zhao and Y. Zhao, *Nano Lett.*, 2010, **10**, 4750–4755.
32 H. Yamada, K. Tagawa, M. Komatsu, I. Moriguchi and T. Kudo, *J. Phys. Chem. C*, 2007, **111**, 8397–8402.
33 A. Sakunthala, M. V. Reddy, S. Selvasekarapandian, B. V. R. Chowdari and P. C. Selvin, *Energy Environ. Sci.*, 2011, **4**, 1712–1725.
34 F. Coustier, S. Passerini and W. Smyrl, *Solid State Ionics*, 1997, **100**, 247–258.
35 F. Coustier, *J. Electrochem. Soc.*, 1999, **146**, 1355–1360.
36 H. Park, *Solid State Ionics*, 2005, **176**, 307–312; D. M. Yu, S. T. Zhang, D. W. Liu, X. Y. Zhou, S. H. Xie, Q. F. Zhang, Y. Y. Liu and G. Z. Cao, *J. Mater. Chem.*, 2010, **20**, 10841–10846.
37 H. Yu, X. Rui, H. Tan, J. Chen, X. Huang, C. Xu, W. Liu, D. Y. W. Yu, H. H. Hng, H. E. Hoster and Q. Yan, *Nanoscale*, 2013, **5**, 4937–4943.
38 Y. Li, J. Yao, E. Uchaker, M. Zhang, J. Tian, X. Liu and G. Cao, *J. Phys. Chem. C*, 2013, **117**, 23507–23514.
39 J. G. Radich, Y.-S. Chen and P. V. Kamat, *ECS J. Solid State Sci. Technol.*, 2013, **2**, M3178–M3181.
40 T. Herricks, J. Y. Chen and Y. N. Xia, *Nano Lett.*, 2004, **4**, 2367–2371.
41 K. T. Lee and J. Cho, *Nano Today*, 2011, **6**, 28–41.
42 E. Frabetti, G. A. Deluga, W. H. Smyrl and M. Giorgetti, *J. Phys. Chem. B*, 2004, **108**, 3765–3771.
43 M. Giorgetti, M. Berrettoni and W. H. Smyrl, *Chem. Mater.*, 2007, **19**, 5991–6000.
44 Q.-H. Wu, A. Thissen and W. Jaegermann, *Surf. Sci.*, 2005, **578**, 203–212.
45 Q.-H. Wu, A. Thissen, W. Jaegermann and M. Liu, *Appl. Surf. Sci.*, 2004, **236**, 473–478.
46 D. Liu, Y. Liu, A. Pan, K. P. Nagle, G. T. Seidler, Y.-H. Jeong and G. Cao, *J. Phys. Chem. C*, 2011, **115**, 4959–4965.
47 J.-T. Li, J. Światowska, V. Maurice, A. Seyeux, L. Huang, S.-G. Sun and P. Marcus, *J. Phys. Chem. C*, 2011, **115**, 7012–7018.
48 B. Wiley, T. Herricks, Y. G. Sun and Y. N. Xia, *Nano Lett.*, 2004, **4**, 1733–1739.
49 Y. G. Sun and Y. N. Xia, *Adv. Mater.*, 2002, **14**, 833–837.
50 P. Ragupathy, S. Shivakumara, H. N. Vasan and N. Munichandraiah, *J. Phys. Chem. C*, 2008, **112**, 16700–16707.
51 Y. Liu, E. Uchaker, N. Zhou, J. Li, Q. Zhang and G. Cao, *J. Mater. Chem.*, 2012, **22**, 24439–24445.
52 K.-S. Hwang, J.-H. Jeong, J.-H. Ahn and B.-H. Kim, *Ceram. Int.*, 2006, **32**, 935–937.